Negative local resistance caused by viscous electron backflow in graphene

D. A. Bandurin[1], I. Torre[2,3], R. Krishna Kumar[1,4], M. Ben Shalom[1,5], A. Tomadin[6], A. Principi[7], G. H. Auton[5], E. Khestanova[1,5], K. S. Novoselov[5], I. V. Grigorieva[1], L. A. Ponomarenko[1,4], A. K. Geim[1], M. Polini[3]

[1]School of Physics & Astronomy, University of Manchester, Oxford Road, Manchester M13 9PL, United Kingdom
[2]National Enterprise for nanoScience and nanoTechnology, Scuola Normale Superiore, I-56126 Pisa, Italy
[3]Istituto Italiano di Tecnologia, Graphene labs, Via Morego 30 I-16163 Genova (Italy)
[4]Physics Department, Lancaster University, Lancaster LA14YB, United Kingdom
[5]National Graphene Institute, University of Manchester, Manchester M13 9PL, United Kingdom
[6]National Enterprise for nanoScience and nanoTechnology, Istituto Nanoscienze-Consiglio Nazionale delle Ricerche and Scuola Normale Superiore, I-56126 Pisa, Italy
[7]Radboud University, Institute for Molecules and Materials, NL-6525 AJ Nijmegen, The Netherlands

Graphene hosts a unique electron system in which electron-phonon scattering is extremely weak but electron-electron collisions are sufficiently frequent to provide local equilibrium above liquid nitrogen temperature. Under these conditions, electrons can behave as a viscous liquid and exhibit hydrodynamic phenomena similar to classical liquids. Here we report strong evidence for this transport regime. We find that doped graphene exhibits an anomalous (negative) voltage drop near current injection contacts, which is attributed to the formation of submicrometer-size whirlpools in the electron flow. The viscosity of graphene's electron liquid is found to be ≈ 0.1 m^2 s^{-1}, an order of magnitude larger than that of honey, in agreement with many-body theory. Our work shows a possibility to study electron hydrodynamics using high quality graphene.

Collective behavior of many-particle systems that undergo frequent inter-particle collisions has been studied for more than two centuries and is routinely described by the theory of hydrodynamics ($1,2$). The theory relies only on the conservation of mass, momentum and energy and is highly successful in explaining the response of classical gases and liquids to external perturbations varying slowly in space and time. More recently, it has been shown that hydrodynamics can also be applied to strongly interacting quantum systems including ultra-hot nuclear matter and ultra-cold atomic Fermi gases in the unitarity limit (3-6). In principle, the hydrodynamic approach can also be employed to describe many-electron phenomena in condensed matter physics (7-13). The theory becomes applicable if electron-electron scattering provides the shortest spatial scale in the problem such that $\ell_{ee} \ll W, \ell$ where ℓ_{ee} is the electron-electron scattering length, W the characteristic sample size, $\ell \equiv v_F \tau$ the mean free path, v_F the Fermi velocity, and τ the mean free time with respect to momentum-non-conserving collisions such as those involving impurities, phonons, etc. The above inequalities are difficult to meet experimentally. Indeed, at low temperatures (T) ℓ_{ee} varies approximately as $\propto T^{-2}$ reaching a micrometer scale at liquid-helium T (14), which necessitates the use of ultra-clean systems to satisfy $\ell_{ee} \ll \ell$. At higher T, electron-phonon scattering rapidly reduces ℓ. However, for two-dimensional (2D) systems with dominating acoustic phonon scattering, ℓ decays only as $\propto T^{-1}$, slower than ℓ_{ee}, which should in principle allow the hydrodynamic description over a certain temperature range, until other phonon-mediated processes become important. So far, there has been little evidence for hydrodynamic electron transport. An exception is an early work on 2D electron gases in ballistic devices ($\ell \sim W$) made from GaAlAs heterostructures (15). They exhibited nonmonotonic changes in differential resistance as a function of a large applied current I that was used to increase the electron temperature (making ℓ_{ee} short) while the lattice temperature remained low (allowing long ℓ). The nonmonotonic behavior was attributed to the Gurzhi effect, a transition between Knudsen ($\ell_{ee} \gg \ell$) and viscous electron flows ($7,15$). Another possible hint for electron hydrodynamics comes from one of

2

the explanations (*16,17*) for the Coulomb drag measured between two graphene sheets at the charge neutrality point (CNP).

Here we address electron hydrodynamics by using a special measurement geometry (Fig. 1) that amplifies effects of the shear viscosity ν and, at the same time, minimizes a contribution from ballistic effects that can occur not only in the Knudsen regime but also for viscous flow in graphene. A viscous flow can lead to vortices appearing in the spatial distribution of the steady-state current (Fig. 1, A and B). Such 'electron whirlpools' have a spatial scale $D_\nu = \sqrt{\nu\tau}$, which depends on electron-electron scattering through ν and on the electron system's quality through τ (*18*). To detect the whirlpools, electrical probes should be placed at a distance comparable to D_ν. By using single- and bi- layer graphene (SLG and BLG, respectively) encapsulated between boron nitride crystals (*19-21*), we could reach D_ν of 0.3-0.4 μm thanks to high viscosity of graphene's Fermi liquid and its high carrier mobility μ even at high T. Such large D_ν still necessitates submicron resolution to probe the electron backflow. To this end, we fabricated multiterminal Hall bars with narrow (≈ 0.3 μm) and closely spaced (≈ 1 μm) voltage probes (Fig. 1C and *fig. S1*). For details of device fabrication, see (*18*).

All our devices were first characterized in the standard geometry by applying I along the main channel and using side probes for voltage measurements. A typical behavior of longitudinal conductivity σ_{xx} at a few characteristic T of interest is shown in Fig. 1D. At liquid-helium T, the devices exhibited $\mu \sim$ 10-50 m^{2}V^{-1}s^{-1} over a wide range of carrier concentrations $n \sim 10^{12}$ cm^{-2}, and μ remained above 5 m^{2}V^{-1}s^{-1} up to room T (*fig. S2*). Such μ allow ballistic transport with $\ell > 1$ μm at $T < 300$ K. On the other hand, at $T \geq 150$ K ℓ_{ee} decreases down to 0.1-0.3 μm over the same range of n (*22, 23* and *figs. S3-S4*). This allows the essential condition for electron hydrodynamics ($\ell_{ee} \ll W, \ell$) to be satisfied within this temperature range. If one uses the conventional longitudinal geometry of electrical measurements, it turns out that viscosity has little effect on σ_{xx} (*figs. S5-S7*) essentially because the

flow in this geometry is uniform whereas the total momentum of the moving Fermi liquid is conserved in electron-electron collisions (*18*). The only evidence for hydrodynamics we could find in the longitudinal geometry was the Gurzhi effect that appeared as a function of the electron temperature controlled by applying large I, similar to the observations of ref. *15* (*fig. S8*).
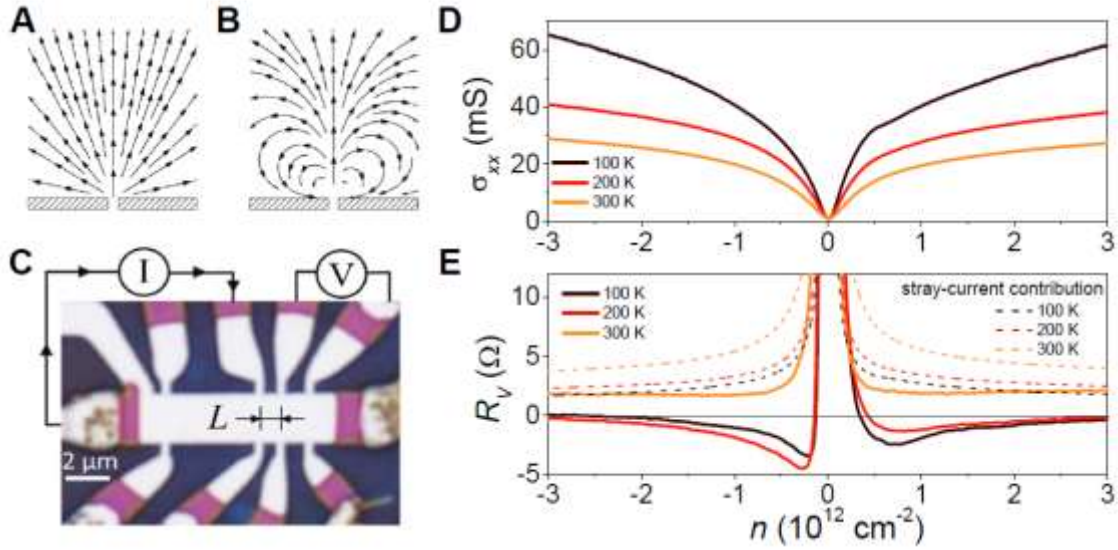
Fig. 1. Viscous backflow in doped graphene. (**A**,**B**) Calculated steady-state distribution of current injected through a narrow slit for a classical conducting medium with zero v (A) and a viscous Fermi liquid (B). (**C**) Optical micrograph of one of our SLG devices. The schematic explains the measurement geometry for vicinity resistance. (**D,E**) Longitudinal conductivity σ_{xx} and R_V as a function of n induced by applying gate voltage. $I = 0.3\ \mu\text{A}$; $L = 1\ \mu\text{m}$; W=?; The dashed curves in (E) show the contribution expected from classical stray currents in this geometry (*18*).

To reveal hydrodynamics effects, we employed the geometry shown in Fig. 1C. In this case, I is injected through a narrow constriction into the graphene bulk, and the voltage drop V_V is measured at the nearby side contacts located at the distance $L \sim 1\ \mu\text{m}$ away from the injection point. This can be considered as nonlocal measurements, although stray currents are not exponentially small (dashed curves in Fig. 1E). To distinguish from the proper nonlocal geometry (*24*), we refer to the linear-response

signal measured in our geometry as "vicinity resistance", $R_V = V_V/I$. The idea is that, in the case of a viscous flow, whirlpools emerge as shown in Fig. 1B, and their appearance can then be detected as sign reversal of V_V, which is positive for the conventional current flow (Fig. 1A) and negative for viscous backflow (Fig. 1B). Figure 1E shows examples of R_V for the same SLG device as in Fig. 1D, and other SLG and BLG devices exhibited similar behavior (18). Away from the CNP, R_V is indeed negative over a wide range of intermediate T, despite a significant offset expected due to stray currents. Figure 2 details our observations further by showing maps $R_V(n, T)$ for SLG and BLG. The two Fermi liquids exhibited somewhat different behavior reflecting their different electronic spectra but R_V was negative over a large range of n and T for both of them. Two more R_V maps are provided in *fig. S9*. In total, seven multiterminal devices with W from 1.5 to 4 μm were investigated showing the vicinity behavior that was highly reproducible for both different contacts on a same device and different devices, independently of their W, although we note that the backflow was more pronounced for devices with highest μ and lowest charge inhomogeneity.
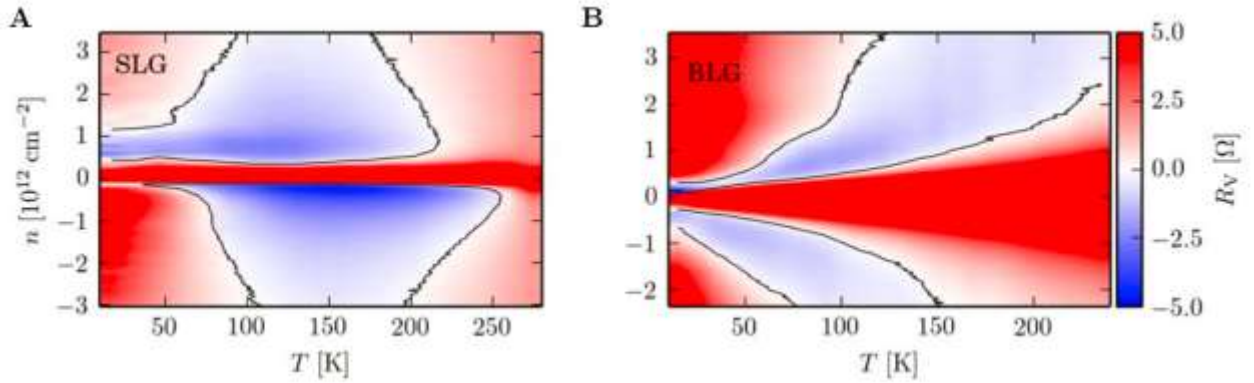
Fig. 2. Vicinity resistance maps. (A, B) $R_V(n, T)$ for SLG and BLG, respectively; the same color coding for the R_V scale. The black curves indicate zero R_V. For each n away from the CNP, there is a wide range of T over which R_V is negative. All measurements presented in this work for BLG were taken with zero displacement between the graphene layers (18).

5

The same anomalous vicinity response could also be observed if we followed the recipe of (*15*) and used the current I to increase the electron temperature. In this case, V_V changed its sign as a function of I from positive to negative to positive again, reproducing the behavior of R_V with increasing T of the cryostat (*fig. S10*). Comparing *figs. S8* and *S10*, it is clear that the vicinity geometry strongly favors the observation of hydrodynamics effects so that the measured vicinity voltage changed its sign whereas in the standard geometry the same viscosity led only to relatively small changes in dV/dI. We also found that the magnitude of negative R_V decayed rapidly with L (*fig. S11*), in agreement with the finite size of electron whirlpools (see below).

Negative resistances can in principle arise from other effects such single-electron ballistic transport ($\ell_{ee} \gg \ell$) or quantum interference (*18,20,24*). The latter contribution is easily ruled out because quantum corrections rapidly wash out at $T > 20$ K and have a random sign that rapidly oscillates as a function of magnetic field. Also, our numerical simulations using the Landauer-Büttiker formalism and the realistic device geometry showed that no negative resistance could be expected for the vicinity configuration in zero magnetic field (*19,21*). Nonetheless, we carefully considered any 'accidental spillover' of single-electron ballistic effects into the vicinity geometry from the point of view of experiment. The dependences of the negative vicinity signal on T, n, I and the device geometry allowed us to unambiguously rule out any such contribution as discussed in (*18*). For example, the single-electron ballistic phenomena should become more pronounced for longer ℓ (that is, with decreasing T or the electron temperature and with increasing n), in stark contrast to the nonmonotonic behavior of V_V.

Now we turn to theory and show that negative R_V arises naturally from whirlpools that appear in a viscous Fermi liquid near current-injecting contacts. As discussed in (*18*), electron transport for sufficiently short ℓ_{ee} can be described by the hydrodynamic equations

$$\nabla \cdot J(r) = 0 \tag{1}$$

and

$$\frac{\sigma_0}{e} \nabla \phi(r) + D_v^2 \nabla^2 J(r) - J(r) = 0 \tag{2}$$

where $J(r) = nv(r)$ is the (linearized) particle current density, and $\phi(r)$ is the electric potential in the 2D plane. If $D_v \to 0$, Eq. 2 yields Ohm's law, $-eJ(r) = \sigma_0 E(r)$ with a Drude-like conductivity, $\sigma_0 \equiv ne^2\tau/m$ where $-e$ and m are the electron charge and the effective mass, respectively. The three terms in Eq. 2 describe: the electric force generated by the steady-state charge distribution in response to applied current I, the viscous force (1,2), and friction caused by momentum non-conserving processes parametrized by the scattering time $\tau(n, T)$.
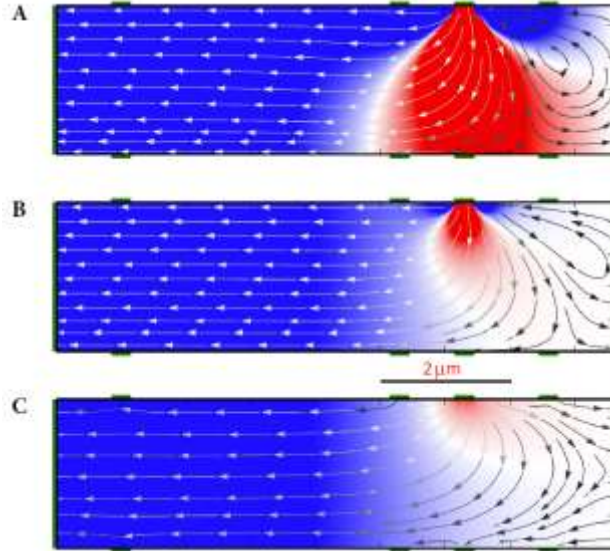
Fig. 3. Whirlpools in electron flow. (**A-C**) Calculated $J(r)$ and $\phi(r)$ for the geometry shown in Fig. 1C, with the green bars indicating voltage contacts. The color scale is for ϕ (red to blue corresponds to $\pm I/\sigma_0$). D_v = 2.3, 0.7 and 0 μm for panels A to C, respectively. Vortices are seen in the top right corners of A and B where the current flow is in the direction opposite to that in (C) that shows the case of zero viscosity. In each panel, the current streamlines also change color from white to black indicating that the current density $|J(r)|$ is lower to the right of the injecting contact.

Equations 1 and 2 can be solved numerically (*18*), and Fig. 3 shows examples of spatial distributions of $\phi(r)$ and $J(r)$. For experimentally relevant values of D_v, a vortex appears in the vicinity of the current-injecting contact. This is accompanied by the sign reversal of $\phi(r)$ at the vicinity contact on the right of the injector, which is positive in Fig. 3C (no viscosity) but becomes negative in Figs. 3, A and B. Our calculations for this geometry reveal that R_V is negative for $D_v \gtrsim 0.4$ μm (*18*). Because both τ and ν decrease with increasing T, D_v also decreases, and stray currents start to dominate the vicinity response at high T. This explains why R_V in Figs. 1 and 2 becomes positive close to room T, even though our hydrodynamic description has no high-temperature cutoff. Note that despite positive R_V the viscous contribution remains quite significant near room T (Fig. 1D, *fig. S12*). On the other hand, at low T the electron system approaches the Knudsen regime and our hydrodynamic description becomes inapplicable because $\ell_{ee} \sim \ell$ (*18*). In the latter regime, the whirlpools should disappear and R_V become positive, in agreement with the experiment and our numerical simulations based on the Landauer-Büttiker formalism.

The numerical results in Fig. 3 can be understood if we rewrite Eqs. 1 and 2 as

$$J(r) = \frac{\sigma_0}{e}\nabla\phi(r) - nD_v^2\nabla \times \boldsymbol{\omega}(r) , \tag{3}$$

where $\boldsymbol{\omega}(r) \equiv n^{-1}\nabla \times J(r) = \omega(r)\hat{z}$ is the vorticity (*2*). Taking the curl of Eq. 3, the vorticity satisfies the equation $\omega(r) = D_v^2\nabla^2\omega(r)$ where D_v plays the role of a diffusion constant. Current I injects vorticity at the source contact, which then exponentially decays over the length scale D_v. For $L = 1$ μm, $\nu = 0.1$ m^2 s^{-1} and $\tau = 1.5$ ps (*18*), we find $D_v \approx 0.4$ μm, in qualitative agreement with the measurements in *fig. S11*.
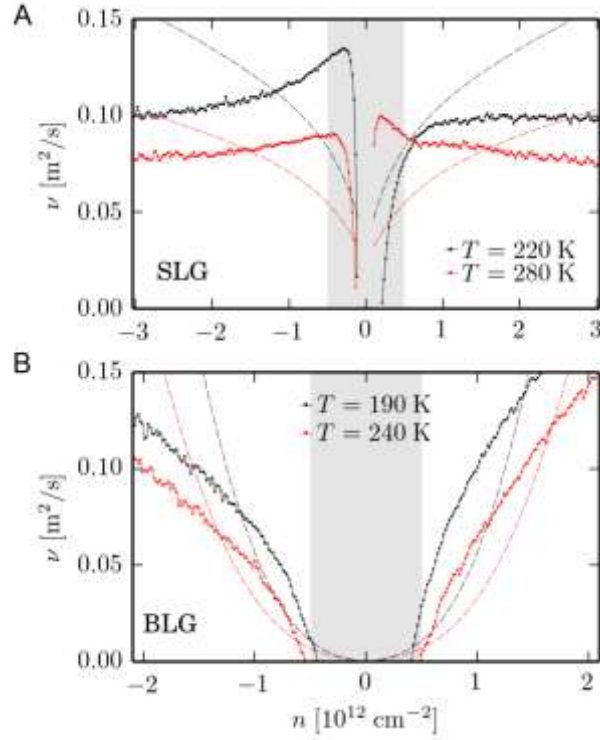
Fig. 4. Viscosity of the Fermi liquids in graphene. (A,B) Solid curves: ν extracted from the experiment for SLG and BLG, respectively. Dashed: Calculations based on many-body diagrammatic perturbation theory (no fitting parameters). The grey-shaded areas indicate regions around the CNP where our hydrodynamic model is not applicable (*18*).

Finally, we combine the measurements of R_V and ρ_{xx} with the solution of Eqs. 1 and 2 in Fig. 3 to extract the kinematic viscosity for SLG and BLG. Because the observed Gurzhi effect in ρ_{xx} is small at low currents (*fig. S6*), we can use $\rho_{xx} = 1/\sigma_0 = m/(ne^2\tau)$ to determine $\tau(n,T)$ (*18*). Furthermore, for the experimentally relevant values of D_ν, we find that R_V is a quadratic function of D_ν

$$R_V = (b + a\, D_\nu^2)\sigma_0^{-1} \tag{4}$$

where a and b are numerical coefficients dependent only on the measurement geometry and boundary conditions and b describes the contribution from stray currents (*fig. S14?*). For the specific device in Fig. 3, we determine $a = -0.29$ μm^{-2} and $b = 0.056$, and this allows us to estimate $D_\nu(n,T)$

from measurements of R_V. For the known τ and D_ν, we find $\nu(n,T) = D_\nu^2/\tau$. Applicability limits of this analysis are discussed in (18), and the results are plotted in Fig. 4 for one of our devices. It shows that, at carrier concentrations $\sim 10^{12}\,\text{cm}^{-2}$ the Fermi liquids in both SLG and BLG are highly viscous with $\nu \approx 0.1\ \text{m}^2\text{s}^{-1}$. For the sake of comparison, liquid honey has typical viscosities of $\approx 0.002\text{-}0.005\ \text{m}^2\text{s}^{-1}$.

Figure 4 also plots results of fully-independent microscopic calculations of $\nu(n,T)$, which were carried out by extending the many-body theory of ref. *(25)* to the case of 2D electron liquids hosted by SLG and BLG. Within the range of applicability of our analysis in Fig. 4 ($n \sim 10^{12}\,\text{cm}^{-2}$), the agreement in absolute values of the electron viscosity is notable , especially taking into account that no fitting parameters were used in the calculations. Because the strong inequality $\ell \gg \ell_{ee}$ required by the hydrodynamic theory cannot be reached even for graphene, it would be unreasonable to expect better agreement (*18*). In addition, our analysis does not apply near the CNP because the theory neglects contributions from thermally-excited carriers, spatial charge inhomogeneity and coupling between charge and energy flows, which can play a substantial role at low doping (*16,18*). Further work is needed to understand electron hydrodynamics in the intermediate regime $\ell \gtrsim \ell_{ee}$ and, for example, explain ballistic transport ($\ell > W$) in graphene at high T in terms of suitably modified hydrodynamic theory. Indeed, the naïve single-particle description that is routinely used for graphene's ballistic phenomena even above 200 K (*19,21*) cannot be justified; a more complete theoryneeds to incorporate the physics of electron-liquid jets. As for experiment, the highly viscous Fermi liquids in graphene and their accessibility offer a tantalizing prospect of using various scanning probes for visualization and further understanding of electron hydrodynamics.

References and Notes:
1. L. D. Landau, E. M. Lifshitz. *Fluid Mechanics.* Pergamon, New York, 1987.
2. G. K. Batchelor. *An Introduction to Fluid Dynamics*. Cambridge University Press, Cambridge, 1967.
3. B. V. Jacak, B. Müller. The exploration of hot nuclear matter. *Science* **337**, 310-314 (2012).

4. C. Cao *et al*. Universal quantum viscosity in a unitary Fermi gas. *Science* **331**, 58-61 (2011).

5. E. Elliott, J. A. Joseph, J. E. Thomas. Anomalous minimum in the shear viscosity of a Fermi gas. *Phys. Rev. Lett.* **113**, 020406 (2014).

6. T. Schäfer, D. Teaney. Nearly perfect fluidity: from cold atomic gases to hot quark gluon plasmas. *Rep. Prog. Phys.* **72**, 126001 (2009).

7. R. N. Gurzhi. Hydrodynamic effects in solids at low temperature. *Sov. Phys. Uspekhi* **11**, 255-270 (1968).

8. A. O. Govorov, J. J. Heremans. Hydrodynamic effects in interacting Fermi electron jets. *Phys. Rev. Lett.* **92**, 026803 (2004).

9. R. Bistritzer, A. H. MacDonald. Hydrodynamic theory of transport in doped graphene. *Phys. Rev. B* **80**, 085109 (2009).

10. M. Müller, J. Schmalian, L. Fritz. Graphene: a nearly perfect fluid. *Phys. Rev. Lett.* **103**, 025301 (2009).

11. A. V. Andreev, S. A. Kivelson, B. Spivak. Hydrodynamic description of transport in strongly correlated electron systems. *Phys. Rev. Lett.* **106**, 256804 (2011).

12. A. Tomadin, G. Vignale, M. Polini. Corbino disk viscometer for 2D quantum electron liquids. *Phys. Rev. Lett.* **113**, 235901 (2014).

13. B. N. Narozhny, I. V. Gornyi, M. Titov, M. Schütt, A. D. Mirlin. Hydrodynamics in graphene: linear-response transport. *Phys. Rev. B* **91**, 035414 (2015).

14. G. F. Giuliani, G. Vignale. *Quantum Theory of the Electron Liquid*. Cambridge University Press, Cambridge, 2005.

15. M. J. M. de Jong, L. W. Molenkamp. Hydrodynamic electron flow in high-mobility wires. *Phys. Rev. B* **51**, 13389 (1995).

16. J. C. W. Song, L. S. Levitov. Energy-driven drag at charge neutrality in graphene. *Phys. Rev. Lett.* **109**, 236602 (2012).

17. R. V. Gorbachev *et al*. Strong Coulomb drag and broken symmetry in double-layer graphene. *Nature Phys.* **8**, 896-901 (2012).

18. See supporting material on *Science* Online.

19. A. S. Mayorov *et al*. Micrometer-scale ballistic transport in encapsulated graphene at room temperature. *Nano Lett.* **11**, 2396-2399 (2011).

20. L. Wang *et al*. One-dimensional electrical contact to a two-dimensional material. *Science* **342**, 614-617 (2013).

21. T. Taychatanapat, K. Watanabe, T. Taniguchi, P. Jarillo-Herrero. Electrically tunable transverse magnetic focusing in graphene. *Nature Phys.* **9**, 225-229 (2013).

22. Q. Li, S. Das Sarma. Finite temperature inelastic mean free path and quasiparticle lifetime in graphene. *Phys. Rev. B* **87**, 085406 (2013).

23. M. Polini, G. Vignale. The quasiparticle lifetime in a doped graphene sheet. *arXiv:1404.5728* (2014).

24. D. A. Abanin *et al*. Giant nonlocality near the Dirac point in graphene. *Science* **332**, 328-330 (2011).

25. A. Principi, G. Vignale, M. Carrega, M. Polini. Bulk and shear viscosities of the 2D electron liquid in a doped graphene sheet. *arXiv:1506.06030* (2015).